HARMONIC LAUNCHING OF ION BERNSTEIN WAVES VIA MODE TRANSFORMATION

BY

M. ONO, K.L. WONG, AND
G.A. WURDEN

JUNE 1982

PLASMA PHYSICS LABORATORY

PRINCETON UNIVERSITY
PRINCETON, NEW JERSEY

PREPARED FOR THE U.S. DEPARTMENT OF ENERGY,
UNDER CONTRACT DE-AC02-76-CHO-3073.

Harmonic Launching of Ion Bernstein Waves Via Mode Transformation

M. Ono, K. L. Wong, and G. A. Wurden

Plasma Physics Laboratory, Princeton University
Princeton, New Jersey 08543

ABSTRACT

Ion Bernstein wave excitation and propagation via finite ion-Larmor-radius mode-transformation are investigated theoretically and experimentally. It is shown that in the ion cyclotron range of frequencies $\omega \lesssim 4\Omega_i$, with modest ion temperatures ($T_i \lesssim 10$ eV), the finite-Larmor-radius effect removes the wave singularity at lower-hybrid resonance layer, enabling an externally initiated electron plasma wave to transform continuously into an ion Bernstein wave. In an ACT-1 hydrogen plasma ($T_e \simeq 2.5$ eV, $T_i \lesssim 2.0$ eV), externally excited ion Bernstein waves have been observed for $\omega \lesssim 2\Omega_i$ as well as for $\omega < 3\Omega_i$. The finite ion-Larmor-radius mode transformation process resulting in strong ion Bernstein wave excitation has been experimentally verified. Detailed measurements of the wave dispersion relation and of the wave-packet trajectory show excellent agreement with theory. The dependence of the excited ion Bernstein wave on the antenna phasing, the plasma density, and on the neutral pressure (T_i) is also investigated. The present work provides information relevant to the physics of ion Bernstein wave propagation and waveguide coupling, as well as to the rf-plasma interaction during ion-cyclotron-range-of-frequency heating in fusion plasmas.

I. Introduction

Application of radiofrequency power near the ion cyclotron range of frequencies and also near the lower-hybrid frequency offers a promising outlook for heating fusion plasmas to ignition temperatures. In this frequency range, radiofrequency (or microwave) power is readily available and relatively inexpensive. One of the most intensely investigated radiofrequency heating phenomena in recent years is the mode-conversion (transformation) process, arising from the finite ion-Larmor-radius effect near the cold plasma resonances.[1-6] This process affects the wave dispersion relation near the resonances and can profoundly influence the overall rf heating efficiencies. As the heating regimes move closer to hotter and denser reactor-like plasmas, the finite ion-Larmor-radius effect plays an increasingly important role in determining the physics of the heating waves.

Recently, it was proposed that a waveguide-launched ion Bernstein wave may offer an attractive alternative method for heating fusion plasmas to ignition temperatures.[7,8] By means of a finite-Larmor-radius transformation process, excellent waveguide coupling and wave accessibility can be achieved in fusion plasmas. Detailed theoretical work on waveguide-coupling, ray tracing, and damping suggests that this heating scheme becomes increasingly attractive as the

plasma and device parameters move toward the reactor regime. For the ion cyclotron range of frequency fast-wave heating due to the relatively large antenna electric field, external excitation of electrostatic waves can also play an important role in the physics of rf-plasma interactions, in particular on the plasma antenna loading and surface heating.

In the present work, we investigate the physics of ion Bernstein wave excitation and propagation via the finite Larmor-radius mode transformation process in a controlled experimental situation in the ACT-1 toroidal device, where the modest plasma parameters ($n_o \lesssim 10^{11}$ cm^{-3}, $T_e \simeq 3$ eV, and $T_i \lesssim 2$ eV) allow detailed probe measurements of wave properties. The plasma and wave parameters are properly scaled to model fusion plasmas, namely, $T_e \simeq T_i$, $\omega \sim \mathcal{O}(\Omega_i) \gg \nu_{eo}, \nu_{ei} \gg \nu_{ii}, \nu_{io}$, $k_\perp \rho_i \simeq 0.2$-3.0, $\omega/k_\parallel V_{T_e} \simeq 3.0$-5.0, the density is sufficiently high so that $\omega \sim \omega_{pi}$ layer occurs near the antenna, and the hydrogen neutral pressure, $P_H \simeq 10^{-5}$Torr, is acceptably low. Preliminary experimental results on $\omega \lesssim 2\Omega_i$ ion Bernstein wave excitation have been recently reported.[10] In this paper we present a more detailed account of our work including relevant theoretical analysis, experimental set-up and measuring technique, as well as the physics of ion Bernstein wave launching at higher ion cyclotron harmonic frequencies. The plan for the paper is as follows.

We derive wave dispersion relations and describe the relevant theory: In Part II A mode-transformation at

the second harmonic frequency and, in Part II B, mode-transformation at higher harmonic frequencies are discussed. In Part II C, other properties of the ion Bernstein wave relevant to experiments are presented. In Part III A, the overall aspect of the ACT-1 toroidal device and experimental set-up are described and in Part III B, a hydrogen ion concentration measuring technique is described. In Sec. IV, we present experimental results: IV A, ion Bernstein wave propagation and identification measurements; IV B, dependence on antenna phasing; IV C, mode-transformation measurements; IV D, third-harmonic ion Bernstein wave excitation measurement; and IV E, ion temperature measurements using the ion Bernstein wave dispersion relation. In Sec. V, we conclude with a summary and discussion.

II. Theory of Ion Bernstein Wave Excitation

The relevant electrostatic dispersion relation for $\omega = \mathcal{O}(\Omega_i)$ can be expressed as[11]

$$k_\perp^2 K_{xx} + k_\parallel^2 K_{zz} = 0 \ , \tag{1}$$

where

$$K_{xx} = 1 + \sum_\sigma \omega_{p\sigma}^2 \frac{\exp(-\lambda_\sigma)}{\lambda_\sigma} \sum_{n=1}^{\infty} \frac{I_n(\lambda_\sigma) 2n^2}{(n^2\Omega_\sigma^2 - \omega^2)} \ ,$$

and

$$K_{zz} = 1 + 2 \frac{\omega_{pe}^2}{\omega^2} y^2 [1 + yZ(y)] \simeq - \frac{\omega_{pe}^2}{\omega^2} \ .$$

Here, $\lambda_\sigma \equiv k_\perp^2 T_\sigma / m_\sigma \Omega_\sigma^2$ σ designates all species, I_n is the modified Bessel function, $y \equiv (\omega/k_\parallel)(m_e/2T_e)^{1/2}$, and Z is the plasma dispersion function.

A. Mode-Transformation Process for $\omega \lesssim 2\Omega_i$

In order to illuminate the physics of mode-transformation, it is instructive to expand terms in Eq. (1) for small λ_σ which is a good approximation for $\omega \lesssim 2\Omega_i$ excitation. To a leading order in λ_σ Eq. (1) takes on the following form:

$$1 - \frac{k_\perp^2}{k^2} \sum_i \frac{\omega_{pi}^2}{\omega^2 - \Omega_\sigma^2} + \frac{k_\perp^4}{k^2} \sum_i \frac{3\omega_{pi}^2 (T_i/m_i)}{(4\Omega_i^2 - \omega^2)(\omega^2 - \Omega_i^2)} - \frac{k_\parallel^2}{k^2} \frac{\omega_{pe}^2}{\omega^2} = 0 \ , \tag{2}$$

where we have assumed cold electrons [i.e., $\omega/k_{\parallel} >> V_{Te} \equiv (T_e/m_e)^{1/2}$] and neglected the electron terms in K_{xx} since $\omega_{pe}^2/\Omega_e^2 << \omega_{pi}^2/\omega^2 \simeq \omega_{pi}^2/\Omega_i^2$. Equation (2) is a quadratic equation in $k_\perp^2$ which can be expressed as

$$a\, k_\perp^4 + b\, k_\perp^2 - c = 0 \quad , \tag{3}$$

where

$$a = \sum_i \frac{3\omega_{pi}^2 (T_i/m_i)}{(4\Omega_i^2-\omega^2)(\omega^2-\Omega_i^2)} \quad ,$$

$$b = 1 - \sum_i \frac{\omega_{pi}^2}{\omega^2-\Omega_i^2} \quad ,$$

$$c = -\, k_\parallel^2 \left(1 - \frac{\omega_{pe}^2}{\omega^2}\right) \simeq +\, k_\parallel^2 \frac{\omega_{pe}^2}{\omega^2} \quad .$$

The coefficients a, b, and c represent the finite-Larmor-radius (thermal) correction, the cold ion, and the cold electron terms, respectively. Trivially, the solution of Eq. (3) is written as

$$k_\perp^2 = \frac{+b \pm (b^2+4ac)^{1/2}}{2a} \quad . \tag{4}$$

The cold plasma (or lower-hybrid) resonance occurs when b vanishes near $\omega \simeq \omega_{pi}$. We shall now consider the evolution of the wave introduced at the low density plasma edge ($b \simeq 1$) as it propagates toward the lower-hybrid resonance layer ($b \simeq 0$) and beyond ($b < 0$).

For the present case where $\Omega_i < \omega \lesssim 2\Omega_i$, the coefficient "a" is positive, and the propagating root of Eq. (4) can be written as

$$k_\perp^2 = \frac{-b + (b^2+4ac)^{1/2}}{2a} . \qquad (5)$$

The behavior of Eq. (5) is shown in Fig. 1 as a solid curve. In a low density region $b \simeq 1 >> (4ac)^{1/2}$, the wave is an electron plasma wave (EPW) and Eq. (5) can be approximated as

$$k_\perp^2 \simeq \frac{c}{b} \simeq \frac{\omega_{pe}^2}{\omega^2} k_\parallel^2 . \qquad (6)$$

As the wave approaches the resonance so that $b \simeq 0 << (4ac)^{1/2}$, electron plasma wave changes over to a wave with the dispersion relation

$$k_\perp^2 \simeq \left(\frac{|c|}{a}\right)^{1/2} \simeq \left[\left(\frac{m_i}{m_e}\right)\left(\frac{k_\perp^2}{k_\parallel^2}\right)\frac{(4\Omega_i^2-\omega^2)(\omega^2-\Omega_i^2)}{3\omega^2 k_\perp^2 (T_i/m_i)}\right]^{1/2} . \qquad (7)$$

This wave can exist for $b = 0$ because of the ion thermal term, and therefore, this intermediate mode may be termed as a lower hybrid thermal wave. As the wave propagates past the resonance layer into higher density region so that $\omega_{pi}^2 >> \omega^2$, $k_\perp^2$ becomes sufficiently large thereby making the ion terms dominate over the electron term ($|b|^2 > 4ac$). In this region, the wave is an ion Bernstein wave whose approximate dispersion relation can be obtained from Eq. (5) to be

$$k_\perp^2 \simeq \frac{|b|}{a} \simeq \sum_i \frac{\omega_{pi}^2}{\omega^2-\Omega_i^2} \Big/ \sum_i \frac{3\omega_{pi}^2 (T_i/m_i)}{(4\Omega_i^2-\omega^2)(\omega^2-\Omega_i^2)} \ . \qquad (8)$$

As can be seen from Fig. 1, an externally launched electron plasma wave connects smoothly onto the ion Bernstein wave via a lower-hybrid thermal wave. Propagating further into the plasma toward higher magnetic field region causes $k_\perp \rho_i$ to increase and requires the inclusion of the higher order terms in Eq. (1) which then can be solved numerically.

In analyzing the above mode-transformation process, we have used a uniform plasma theory which requires the WKB approximation (i.e., $\partial k_\perp / \partial r \; k_\perp^{-2} << 1$) to be satisfied in the mode-transformation region ($b \simeq 0$). Using Eq. (7) one can obtain an inequality for the WKB condition

$$\frac{\partial k_\perp}{\partial x} \frac{1}{k_\perp^2} \simeq \frac{1}{4k_\perp} \left[\frac{\partial T_i}{\partial x} \frac{1}{T_i} \right] \simeq \frac{\lambda_\perp}{8\pi L} << 1 \ , \qquad (9)$$

where L is the ion temperature gradient scale length. It is interesting to note that in this region, due to the weak density dependence of the wave dispersion relation in Eq. (7), the important gradient scale length is that of the ion temperature. Since $\lambda_\perp$ is typically $\lesssim$ 1 cm and L is larger than 1 mm in almost any experimental situation , the WKB treatment of the present mode-transformation process is justified, and no wave reflection should occur.

As a comparison, we briefly consider the well-known lower hybrid heating case where $\omega >> \Omega_i$. In this case, the thermal coefficient "a" is negative, and the propagating solutions exist only for $b > (4|a|c)^{1/2}$. From Eq. (4) we obtain

$$k_\perp^2 \simeq \frac{b \mp (b^2 - 4|a|c)^{1/2}}{2|a|} . \tag{10}$$

The upper-root represents the initially launched electron plasma wave

$$k_\perp^2 \simeq \frac{b - (b^2 - 4|a|c)^{1/2}}{2|a|} \simeq \frac{c}{b} \simeq \frac{\omega_{pe}^2}{\omega^2} k_\parallel^2 , \tag{11}$$

which then turns around when $b^2 = 4|a|c$ and mode-converts into the lower root, known as a hot-plasma wave[1]

$$k_\perp^2 = \frac{b + (b^2 - 4|a|c)^{1/2}}{2|a|} \simeq \frac{b}{|a|} . \tag{12}$$

In Fig. 1, we plot this conversion process with a dashed curve. Even though the mode-conversion picture shown in Fig. 1 is essentially correct, it should be emphasized that the present WKB treatment for the lower hybrid heating case breaks down near the turning point, and therefore requires a proper treatment of the wave differential equation as investigated in various literatures (Ref. 1,12, and 13).

In Fig. 2(a) we plot $k_\perp$ numerically calculated from Eq. (1) as a function of radial distance x from the antenna for various ion temperatures (as labeled). The wave frequency has been chosen so that $\omega/\Omega_H \simeq 1.9$ at $x = 0$. Density increases linearly with x, and when $x \simeq 1$ cm the lower hybrid resonance ($b = 0$) is encountered. Magnetic field varies roughly as $1/(R_o + a-x)$ and therefore increases with x. The corresponding value of ω/Ω_H is indicated by the top scale in the figure. The cold plasma case ($T_i = 0$) shows propagation for $b > 0$, then resonance ($k_\perp^2 \to \infty$) at $b = 0$. The wave is evanescent ($k_\perp^2 < 0$) for $b < 0$. For finite ion temperature, the singular behavior at the lower hybrid resonance disappears, and the wave number changes smoothly from electron plasma wave to the ion Bernstein wave region. The ion Bernstein wave number decreases for increased T_i, and the change in $k_\perp$ associated with mode-transformation decreases accordingly. In Fig. 2(b), the corresponding wave trajectories are shown. As expected for the warm-ion case, the lower hybrid resonance has almost no effect on the wave trajectories enabling the wave to propagate continuously through the cold plasma resonance.

B. Mode-Transformation at Higher Harmonic Frequencies.

Mode-transformation into IBW can occur for higher ion cyclotron harmonic frequencies. This occurs due to the effect of higher-order ion-Larmor-radius terms in the wave dispersion relation and, thus, requires progressively warmer ion temperatures. To illuminate the physics of mode-transformation process,

it is helpful to rewrite Eq. (1) in the form

$$\frac{\omega_{pi}^2 \exp(-\lambda_i)}{\lambda_i} \sum_{n=m}^{\infty} \frac{I_n(\lambda_i) 2n^2}{(n^2\Omega_i^2 - \omega^2)} - \frac{\omega_{pi}^2 \exp(-\lambda_i)}{\lambda_i} \sum_{n=1}^{m-1} \frac{I_n(\lambda_i) 2n^2}{\omega^2 - n^2\Omega_i^2}$$

$$+ 1 - \frac{\omega_{pe}^2}{\omega^2} \frac{k_n^2}{k^2} = 0 \ , \qquad (13)$$

where $m\Omega_i \gtrsim \omega > (m-1)\Omega_i$, and to have used single ion species, cold electron plasma ($\omega/k_n V_{T_e} >> 1$). The electron plasma wave dispersion relation [Eq. (6)] is obtained by balancing the last two terms, and the ion Bernstein wave dispersion relation results from balancing the first two ion terms in Eq. (13). Favorable mode-transformation occurs when the first term which is positive becomes dominant over the negative second term near the mode-transformation region. This condition can be satisfied by choosing ω arbitrary close to $m\Omega_i$ such that $1/(m^2\Omega_i^2-\omega^2) \cdot 1/\omega^2\delta >> 1/(\omega^2-\ell^2\Omega_i^2)$ where $\ell < m$ and δ being small. For example, for m = 3, one can choose $\omega \lesssim 3\Omega_i$ and expanding Eq. (13) in λ_i to $\mathcal{O}(\lambda_i^2)$ to obtain

$$d\, k_\perp^6 - |a|\, k_\perp^4 + b\, k_\perp^2 - C = 0 \ , \qquad (14)$$

where

$$d = \frac{\omega_{pi}^2 (T_i/m_i)^2}{\Omega_i^4} \left[\frac{3}{8} \frac{1}{9\Omega_i^2 - \omega^2} + \frac{1}{\omega^2 - 4\Omega_i^2} - \frac{5}{8(\omega^2 - \Omega_i^2)} \right] ,$$

and a, b, and c are defined in Eq. (3). One can see that d can be positive and sufficiently large, given that ω is near $3\Omega_i$, and $V_{Ti} \equiv (T_i/m_i)^{1/2}$ is reasonably large. Even though Eq. (14) is irreducible in much of the regime of interest, one can readily see how the mode-transformation takes place. In the low density edge, the ion terms can be neglected and the wave is an electron plasma wave. Near the lower hybrid turning point ($k_\perp^2 \sim b/|a|$), the second and third terms cancel each other, yielding a wave dispersion relation given by $k_\perp^2 = (c/d)^{1/3}$. As the wave propagates further, $k_\perp^2$ increases, and the electron term in Eq. (14) becomes relatively small yielding

$$k_\perp^2 = \frac{|a| + (|a|^2 - 4bd)^{1/2}}{2d} . \qquad (15)$$

Equation (15) is a reasonably accurate dispersion relation for IBW in $\omega \lesssim 3\Omega_i$ regime. In this regime, one can show that a condition for smooth transformation, $c \gtrsim |a|^3/4d^2$, can be given by

$$\omega/k_\parallel \lesssim 1.7 \times 10^2 \times V_{Ti}/\delta \ (\text{cm/sec}), \qquad (16)$$

where $\delta = (9\Omega_i^2 - \omega^2)/\omega^2$, or for ACT-1 parameter, $\delta \sim 0.07$, $V_{Ti} \simeq 10^6$ cm/sec ($T_i = 1$ eV), and $f \simeq 18$ MHz, $\lambda_\parallel \sim 135$ cm which is well above the experimental $\lambda_\parallel \simeq 36$ cm. Qualitatively speaking, similar argument can be applied for higher harmonic frequencies.

In Fig. 3(a), we plot numerically calculated $k_\perp$ versus radial position for $\omega \lesssim 3\Omega_i$ and $\lambda_\parallel = 36$ cm for various ion temperatures (as labeled). The wave frequency is chosen such that $\omega/\Omega_H = 2.9$ at the antenna, and a linear density profile is chosen (as in Fig. 2) to place the lower hybrid resonance layer at $x \simeq 1$ cm. As can be seen from the figure, the ion temperature must be roughly three times the second harmonic launching case for similar $k_\perp$ behavior. Corresponding wave trajectories are shown in Fig. 3(b). In Figs. 3(c) and 3(d), similar curves for fourth harmonic ($\omega \lesssim 4\Omega_i$) launching are shown where the excitation requires about an order of magnitude larger ion temperature compared to the second harmonic case. In general, we find for nth harmonic launching, due to the increased $k_\perp \rho_i$ values, the required T_i goes up as $10^{(n/2)-1}$ at the ω_{pi} layer. Therefore, in a tokamak experiment where the edge ion temperature ($\omega \simeq \omega_{pi}$) is $\sim 1/20$ of central temperature, external IBW launching may be practical for a reasonable range of rf frequency, $\omega < 4\Omega_i$.

C. Other Properties of Ion Bernstein Wave

Before going on to the experiment, we briefly describe various properties of ion Bernstein wave[14] which are relevant to the experiment. The ion Bernstein wave, like electron plasma wave, is a backward propagating wave where $\vec{v}_{g\perp}$ is anti-parallel to $\vec{v}_{ph\perp}$. The wave energy (group velocity

direction) flows obliquely to the magnetic field [see Fig. 2(b)], but with angle $\tan\theta \propto V_{Ti}\lambda_{\parallel}$, which is quite different from the electron plasma wave where $\tan\theta \propto n_e^{-1/2}$. The dependence of θ with $\lambda_{\parallel}$ causes the wave packet to spread in radial direction, as opposed to the "resonance cone" behavior of the electron plasma wave.[15] The perpendicular wavelength of the ion Bernstein wave is determined mainly by the local ion temperature and magnetic field. From Eq. (1), one can write for a small electron term (i.e., $\lambda_{\perp}/\lambda_{\parallel}(m_i/m_e)^{1/2} \ll 1$),

$$\frac{\omega}{K_{\perp}} = V_{Ti}\, g(N_i, \frac{\omega}{\Omega_i}), \tag{17}$$

where g is a function with argument N_i and ω/Ω_i. In a single ion species plasma, for $\omega < 2\Omega_i$, from Eq. (8) one obtains

$$\lambda_{\perp} \simeq V_{Ti}\, f^{-1} \left(\frac{3}{4(\Omega_i/\omega)^2 - 1}\right)^{1/2}, \tag{18}$$

where f is the wave frequency. Therefore, in a given magnetic field region, the ion Bernstein perpendicular wavelength is proportional to the ion thermal velocity.

III. Experimental Set-Up and Measurement Techniques

A. ACT-1 Research Torus

The experiments were performed in the Princeton ACT-1 research torus.[16] A schematic of the device is shown in Fig. 4. A steady-state pure toroidal magnetic field of up to 5.5 kG is generated by 26 sets of toroidal field coils with a field ripple along the minor axis of $\lesssim$0.5%. A set of two vertical field coils is installed to provide a small amount of vertical as well as horizontal correction field of $\lesssim$10 G. The vacuum chamber consists of 26 identical wedge-type sections forming a toroidal plasma bore of 59 cm major radius and 10 cm minor radius. Each chamber section contains a large 10 cm × 40 cm port to provide a good access to the plasma. The plasma is produced by a hot tungsten filament plasma source shown in Fig. 5, and the plasma diameter is usually limited to $\lesssim$15 cm by a set of copper limiters. The filament is heated to thermionic emission temperatures, and the emitted electrons are accelerated by a bias voltage (typically 150 volts) applied between the filament and a grounded limiter, acting as an anode. The accelerated electrons circulate around the torus many times before being lost due to ∇B drift. A small vertical field can also be introduced to vary the rate of

vertical drift. The relatively long electron path length (60-300 m) can provide efficient ionization of the background neutral gases. A good stable discharge can be maintained even for as low a gauge neutral pressure as 7×10^{-6} Torr, leaving a warm-ion (~1.5 eV), highly ionized ($\lesssim$ 30%), low collisionality hydrogen plasma with $n_e \lesssim 10^{11}$ cm^{-3}. The guage neutral pressure for hydrogen is about 2.4 times lower than the absolute pressure measured by Baratron. As shown by Fig. 5, the plasma consists of a narrow vertical band of hot electron region near the filament and a diffused plasma region filling the space bounded by the limiter. In the hot electron region, the plasma density measured by a microwave interferometer can be as high as 3×10^{11} cm^{-3}. Since the diffused plasma is free of hot electrons and is nearly Maxwellian, the wave propagation experiments are conducted in this region. Typical radial profiles of the plasma density and temperatures are shown in Fig. 6 (a) and (b). The plasma density is measured by the lower hybrid resonance cone propagation technique and by Langmuir probe ion saturation current. The electron temperature is measured by a Langmuir probe, and the ion temperature profile is obtained from the ion Bernstein wave dispersion relation, which will be discussed in detail in Section IV. The plasma is found to be relatively uniform in the vertical direction. Relative ion concentrations are measured by the low-frequency resonance-cone propagation technique,[17] which will be discussed in the next section. The density fluctuation level $\delta n/n$, measured by the ion saturation current, usually increases toward the plasma edge, and ranges between ~ 5% to 20%.

In Fig. 4, a schematic of wave excitation and detection set-up is shown. Low level rf power (<0.1 watt) with alternate phase is applied to a pair of electrostatic antennas, which are placed one port apart (~16.5 cm) at the outer edge (low-field side) of the plasma, 1/8" to 1/4" behind the plasma limiter. This type of electrostatic antenna has been used previously to excite the electron plasma wave [18,19] and, also, the cold electrostatic ion cyclotron wave.[17] In the present experiment, the excitation frequency was set at $f \simeq 2f_{ci}(H_1^+) \simeq$ 12-14 MHz, corresponding to $B_o \simeq$ 4.0-4.6 kG near the outer plasma edge, and the effective parallel wavelength of the antenna was put at $\lambda_{\parallel} \simeq 34$ cm so that $\omega/k_{\parallel} \simeq 4.0 \times 10^8$ cm/sec $>> (2\,T_e/m_e)^{1/2} \simeq 10^8$ cm/sec. The excited waves were detected by rf probes placed at various toroidal locations.

B. Ion Concentration Measurement

Various ion concentration measuring techniques have been investigated previously in Princeton's L-4 linear research device.[17,20] In particular, it was found that the low-frequency-resonance cone provides a quick and non-perturbing way of measuring the local ion concentrations in the plasma.[17] The low-frequency-resonance cone propagates below each ion cyclotron frequency with a propagation angle (with respect to the local magnetic field line) which depends

primarily on the ion concentrations. One can obtain the dispersion relation from Eq. (1) in the form

$$\theta^2 \frac{m_H}{m_e} = \sum_i \frac{N_i \omega^2 Z_i^2}{A_i\left(\Omega_i^2 - \omega^2\right)} \quad , \tag{19}$$

where $\theta \equiv \tan^{-1}(V_{g_\perp}/V_{g_\parallel}) \simeq \tan^{-1}(k_\parallel/k_\perp)$, N_i is the ion concentrations, Z_i is the ion charge state, and A_i is the ion mass number. In deriving Eq. (19), we have assumed electrons to be cold (i.e., $\omega/k_\parallel > V_{Te}$) and the plasma density is sufficiently high so that $\omega_{pi} > \Omega_i$. A nice feature of Eq. (19) is that the concentration N_i depends only on the cone angle and the local magnetic field. For $\omega \simeq \Omega_i$, one can in most cases neglect other ion terms and use an approximate relation to determine N_i:

$$N_i \simeq \frac{A_i}{Z_i^2}\left(\frac{\Omega_i^2}{\omega^2} - 1\right) \frac{m_H}{m_e}\theta^2 . \tag{20}$$

Equation (20) is a convenient relation to obtain the first order ion concentration before proceeding on to the full solution of Eq. (19).

The resonance cone is excited by the same electrostatic antenna used for the ion Bernstein wave excitation as described in Sec. III (a). The excited resonance cone propagates obliquely to the magnetic field line in a well defined wave packet, which is measured by radially scanning probes placed at various toroidal locations. In Fig. 7 (a),

radial amplitude profiles of the resonance cone launched from the exciters placed 3 ports (top trace) and 6 ports (bottom trace) away from the probe. One should remember that the radially scanned probe intersects both the resonance cones propagating the "short" way and the "long" way around the torus. By measuring the wave packet displacement within a known toroidal distance ΔZ, one can obtain the cone angle $\theta = \tan^{-1}\Delta r/\Delta Z \simeq \Delta r/\Delta Z$. In Fig. 6(b), we show the measured θ as a function of ω/Ω_i in a typical hydrogen discharge plasma used in our experiment. We note that there are three propagating branches which correspond to the presence of three ion-species in the plasma namely, H_1^+, H_2^+, and H_3^+. The relative ion concentrations in this case are 60% H_1^+. 16% H_2^+, and 24% H_3^+. In our hydrogen plasma, we observe H_1^+ to be a dominant ion-species. The ion concentrations are also found to be uniform in the experimental region, within our experimental uncertainty, $\delta N_i/N_i \simeq 20\%$.

IV. Experimental Results

A. Ion Bernstein Wave Propagation and Identification

Figure 8 displays typical radial profiles of the excited ion Bernstein wave amplitude for various axial positions, Z. Here we have defined the radial distance x so that the wave launcher is located at x = 0. Inward propagation of the excited-wave packet is seen as it travels away from the antenna. The cold-plasma resonance, located at x = 1 cm, causes no visible perturbation to the wave trajectory. The wave packet, however, starts to spread after mode-transforming into the ion Bernstein wave, as expected from theory (See Sec. II). To identify the excited wave, we measured perpendicular and parallel wavelengths by interferometry and in Fig. 9(a) typical radial interferometer patterns are shown for several values of ω/Ω_H. The wave exhibits a cutoff ($\lambda_\perp \to \infty$) as ω approaches $2\Omega_H$, and $\lambda_\perp$ decreases with ω for given x. For given ω, the wavelength also decreases with increasing x (decreasing R) which reduces ω/Ω_H.

In Fig. 9(b), where the radial interferometer pattern is shown for various time delays of the boxcar sampler window, the wave phase front moves towards the antenna, confirming the backward-propagating nature of the ion Bernstein wave. In Fig. 9(c), we have plotted the measured wave dispersion relation (dots) at x = 4cm and find excellent agreement with the theoretical curve for T_i = 1.5 eV. The measured parallel

wavelength, $\lambda_{\parallel} \simeq 32\text{-}40$ cm, also agrees reasonably well with the effective antenna wavelength, $\lambda_{\parallel} \simeq 34$ cm. From these measurements we conclude that the excited wave is indeed the ion Bernstein wave.

We recall that in the earlier Q-machine experiments on ion Bernstein wave,[21] it was critical to align the exciter exactly along the magnetic field line to observe the wave excitation. The main difficulty in the Q-machine experiment was in satisfying the cold electron condition, $\omega/k_{\parallel} \sim 2f_{ci}\lambda_{\parallel} > 3(T_e/m_e)^{1/2}$, to avoid strong electron Landau damping. In the experiment, $f_{ci} \sim 200$ kHz ($m_i = 40$) and $(T_e/m_e)^{1/2} \sim 2 \times 10^7$ cm/sec, which then gives the required $\lambda_{\parallel}$ to be larger than 150 cm, comparable to the machine length $L = 100$ cm. In our experiment, this difficulty was minimized by using a hydrogen plasma, $f_{ci} \sim 6$ MHz and $(T_e/m_e)^{1/2} \sim 7 \times 10^7$ cm/sec, which gives the required $\lambda_{\parallel}$ to be only larger than 18 cm, enabling us to use a slow wave structure to launch IBW with well-defined $\lambda_{\parallel}$. We generally find that the ion Bernstein wave is one of the most readily excitable waves with excellent coherence in our warm-ion hydrogen plasma.

Returning to Fig. 8, we have also drawn on this plot ion-Bernstein-wave trajectories calculated using experimental parameters. To account for the spread in $\lambda_{\parallel}$ due to the finiteness of the antenna, trajectories are shown for three values of $\lambda_{\parallel}$. This calculation agrees reasonably well with the observed wave trajectory and explains to some extent the

wave packet spreading. The amplitude modulation of the wave packet in Fig. 8 is apparently an interference phenomenon caused by the interference of the ion Bernstein wave with the near field (electromagnetic) component of the antenna.[15]

By using a vertically movable, horizontally scanning probe, we have investigated the radial phase front of the ion Bernstein wave. In this case, we have used a pair of two straight antennas 12 cm in height placed ~6 mm behind a set of straight limiters. In Fig. 10(a) we show radial interferometry patterns obtained at various vertical positions (as labeled). The wave coherence remains quite good even though the exciter in this case is placed 11 ports away (more than a third of the way around the torus) from the probe. At this point, the wave packet has penetrated radially into the plasma and also has a large radial extent. By connecting the equivalent phase points on the interferometry patterns, one can obtain a radial wave phase front pattern as shown by Fig. 10(b). We observe a coherent phase pattern which retains the original exciter image even near the center of the plasma. The small curvature of the phase front can be attributed to the slightly weaker magnetic field in the upper right region. This type of phase pattern also shows that the vertical variation (T_i, B_o) is relatively small in our plasma.

B. Dependence on Antenna Phasing

Interesting observations can be made when the relative phase of the applied radio frequency signal on the antenna

elements is varied. In Fig. 11, radial amplitude profiles (solid traces) and interferometry output (dashed traces) detected by a probe placed six ports away are shown for the relative antenna phasings of $\phi = 0$ and π. In the top scale of the figure, we have indicated the expected radial positions obtained from ray tracing calculations for various $\lambda_{\perp}$ components (as labeled). For the $\phi = \pi$ case, the wave amplitudes are observed to peak near $\lambda_{\perp} = 36$ cm. in agreement with the measured $\lambda_{\perp}$ excited by the $\phi = \pi$ antenna. When the antenna is driven in-phase ($\phi = 0$), the wave packet spreading is much more enhanced, which indicates much broader $\lambda_{\perp}$ spectrum. We observe for the $\phi = 0$ case, a higher level of evanescent electromagnetic (near field) component represented by the larger surface signal and amplitude modulation. Since the electromagnetic component decays approximately as $\exp(-k_{\perp}x)$ away from the antenna, this observation indicates that the effective antenna $k_{\perp}$-spectrum is smaller (or the decay length longer) for the $\phi = 0$ case, as expected.

We have also utilized four antenna elements, phasing them by $\pi/2$, to generate unidirectional ion Bernstein wave, as shown in Fig. 12(a). This traveling wave configuration should excite ion Bernstein wave propagating preferentially in one toroidal direction depending on the phase being either + or - $\pi/2$. In Fig. 12(b), we show the detected wave radial amplitude profiles for the cases where the wave is launched

toward (upper-trace) and away (lower-trace) from the probe. One observes significantly higher detected wave packet signal when the wave is launched toward the probe. From such measurement, we observe about 80% of the wave power can be launched in the preferred toroidal direction, which is comparable in efficiency to that of the lower hybrid wave.[22] One possible application of the unidirectional IBW is in driving the toroidal current,[23] where the excellent IBW accessibility in hot dense plasmas may make it suitable for driving current in the steady-state high-temperature phase of the reactor operation.

C. Mode-Transformation Process

In ACT-1, by changing the neutral pressure, the hydrogen ion temperature can be varied over a wide range (1/40 eV to 2 eV), and Fig. 13(a) shows the interferometry output for several neutral pressures. For the high-pressure case ($P_H = 4 \times 10^{-4}$ Torr) the ions are essentially cold ($T_i \simeq 1/40$ eV), and the excited wave is the well-known electron plasma wave[19]; the electron plasma wave excited in this region behaves quite like the cold-ion case ($T_i = 0$ curves in Fig. 2), where the wave packet stays near the surface, outside the cold plasma resonance. Strictly speaking, even at $T_i \simeq 1/40$ eV, the mode-transformation should eventually occur into a very short, submillimeter ion Bernstein wave. However, at such short

wavelength, the probe is no longer sensitive, and the wave is likely to be heavily damped by collisions. As the neutral pressure is reduced (T_i increased), the mode-transformed ion Bernstein wave becomes increasingly apparent. As may be seen from Fig. 13(a), the reduction in pressure causes the ion Bernstein wavelength to increase [recall that $\lambda_\perp \propto \sqrt{T_i}$ as in Eq. (17)].

To quantitatively check the mode-transformation process, we have followed the wave packet trajectory and measured the wavenumber as a function of the radial position. In Fig. 13(b), the measured wave number (shown as dots) is plotted as a function of the radial position in a warm-ion plasma in which the plasma density was lowered so that the cold-plasma resonance occurs at $x \simeq 2$ cm. As expected, we observe no sign of discontinuity near the resonance layer. The solid curve is obtained from Eq. (1) for $T_i = 1.5$ eV, and the dashed curve is for $T_i = 0$. The experimental data agrees quite well here with theory, verifying the finite-ion-Larmor-radius mode transformation process. We note that the WKB-approximation is well-satisfied throughout the experimental region.

Next we investigated the effect of plasma density on wave propagation to clearly demonstrate the transition from electron plasma wave ($\omega_{pi} \lesssim \omega$) to ion Bernstein wave regime ($\omega \gtrsim \omega_{pi}$). In Fig. 14(a), the measured wave packet amplitude (heavier curve) and interferogram output (lighter curve)

detected by a radially scanning probe six ports away (~90 cm) from the antenna are shown for various central plasma densities (as labeled). In the figure we have indicated the radial position of the lower hybrid resonance layer which separates electron plasma wave and ion Bernstein wave regimes by a dashed curve. In the low density case ($n_o < 0.7 \times 10^{10}$ cm^{-3}), one can observe the usual two antenna elements electron plasma wave resonance cone and interferogram behavior where the propagation angle ($\tan\theta \propto n_o^{-1/2}$) decreases with increasing density. When the density is raised so that the lower hybrid layer crosses the wave packet ($n_o \simeq 0.7 \times 10^{10}$ cm^{-3}), the finite ion-Larmor-radius effect becomes important and the ion Bernstein wave oscillation starts to emanate from the high density side of the wave packet. As the density is raised further, the wave packet starts to spread and penetrates deeper into the plasma, representing the change-over into the ion Bernstein wave. For $n_o \gtrsim 4.4 \times 10^{10}$ cm^{-3} ($\omega_{pi}^2 \gg \omega^2$), the wave is a fully developed ion Bernstein wave which has the density independent dispersion relation and, accordingly, shows little change in the wave propagation characteristics. We observe in the experiment that the ion Bernstein wave can be launched effectively even when the plasma density is raised so that the ω_{pi} layer reaches the limiter and approaches within few millimeters of the antenna surface. In Fig. 14(b), using corresponding plasma parameters,

the expected ray position obtained from trajectory calculation is shown for various $\lambda_{\parallel}$ (as labeled). One can see that the observed wave packet central position follows the calculated position for $\lambda_{\parallel} \simeq 36$ cm, which is the dominant excited $\lambda_{\parallel}$-spectrum in our experiment. The calculation is also consistent with the observed wave packet spreading, although there is some tendency for the spreading to start at slightly lower density than the theory suggests.

D. Third Harmonic Launching

External launching of IBW at third harmonic frequency has been investigated also. As opposed to the second harmonic launching, coherent excitation of IBW in this frequency range was more difficult due to the higher required ion temperature (Sec. II-B). However, satisfactory launching can be observed when the neutral pressure is lowered and the filament current is increased so that the ion temperature is increased to $\sim$ 2 eV, which is near the maximum ion temperature thus far obtained with the filament source. In Fig. 15(a), we plot the measured IBW dispersion relation at r = 4 cm. Solid curves are theoretical values for various ion temperatures. The measured values agree well with the theoretical curve for $T_i \simeq 2$ eV, which is consistent with the expected ion temperature.

To check for the third harmonic mode-transformation process, we measured the wave number as a function of the distance x from the antenna which is plotted in Fig. 15(b).

The dots are measured values, and the solid curve (T_i = 2 eV) is theoretical value computed using experimentally measured plasma parameters. The cold plasma case (T_i = 0) is shown as a dashed curve for a comparison. As shown by the figure, a smooth continuous mode-transformation does indeed occur, and there are no observable signs of discontinuity near the lower hybrid resonance layer at x ≈ 2.5 cm. This is encouraging considering that this mode-transformation process comes about because of the second order ion-Larmor-radius term [See Eq. (14)], and yet requires a relatively modest ion temperature of ~2 eV. The experimental observation is consistant with theory in that it takes about three times higher ion temperature to achieve similar launching behavior (wavenumber, coherence, etc.) as the second harmonic case. We have not so far observed satisfactory external launching at the fourth harmonic in our plasma because it requires even higher edge ion temperatures.

E. Ion Temperature Measurement Utilizing Ion Bernstein Wave

The coherent propagation property of the ion Bernstein wave can provide a useful hydrogen ion temperature information in the plasma through Eq. (17) [see also Fig. 9(c)]. The ion temperature profile shown in Fig. 6(b) is obtained from the measured ion Bernstein wave dispersion relation. In Fig. 16, we also show the similarly measured ion temperature as a function of the neutral pressure. It is interesting to note

that the ion temperature is roughly related inversely to the neutral pressure which is consistant with the expected ion energy loss mechanism in ACT-1, dominated by the charge-exchange and the ion-neutral collisions. This is also consistant with the previous ion temperature measurement using the electrostatic ion cyclotron wave[20] which also showed the inverse-P dependence.[16]

V. Summary and Discussion

External excitation of ion Bernstein waves has been investigated in a warm-ion hydrogen plasma in the ion cyclotron range of frequencies, $\omega \lesssim 4\Omega_i$. It is shown that the finite ion-Larmor-radius effect permits smooth continuous transformation of an externally initiated electron plasma wave into an ion Bernstein wave through the lower hybrid resonance layer, providing an efficient mechanism for launching ion Bernstein waves. Inclusion of progressively higher-order Larmor-radius terms is needed to describe the physics of IBW launching at the higher harmonic frequencies. Because of the increasingly larger $k_\perp \rho_i$ value at higher harmonic frequencies, to achieve comparable launching at nth harmonic frequency requires the edge ion temperature of approximately $T_i \propto 10^{n/2-1}$.

In an ACT-1 warm ion hydrogen plasma ($T_e \sim 2.5$ eV, $T_i \lesssim 2$ eV, and $n_o \lesssim 10^{11}$ cm^{-3}), the mode-transformation process has been observed for $\omega \lesssim 2\Omega_i$ as well as for $\omega \lesssim 3\Omega_i$, where the

measurements of $k_\perp(\omega,k_\parallel)$ and $k_\perp(x)$ have been found to be in excellent agreement with theory. Effect of antenna phasing, plasma density, and ion temperature on the wave propagation has also been investigated and found to be in good agreement with theory. Efficient ion Bernstein wave excitation is observed over a wide range of plasma parameters even when the density is raised so that the lower hybrid layer is moved to within a few millimeters of the antenna surface.

Efficient mode-transformation of the electron plasma wave into an ion Bernstein wave constitutes the central element of waveguide ion Bernstein wave plasma heating [Ref. 9]. Experimental verification of the wave excitation mechanism puts the waveguide coupling theory as well as the wave accessibility calculations on firmer ground. In particular, the waveguide coupling theory based on the electron plasma wave-ion Bernstein wave mode-transformation process predicts excellent natural coupling of a modest phased waveguide coupler (one or two elements) to the plasma. The absence of a standing wave minimizes the electric field in the waveguide and can reduce rf breakdown problems. This may become an important factor for heating fusion reactors where a large rf power (~100 MW) must be transmitted through a limited aperture opening (~10^5 cm^2). The ability for the IBW to be launched at high harmonics reduces the waveguide size to reasonable values suitable even for intermediate size devices. For example, for a 50-kG device, the waveguide size will assume ~1.3 m for second harmonic launching and ~65 cm for fourth harmonic launching. If a dielectric material

with modest dielectric constant of $\epsilon \simeq 6$ (ceramic) is used, the size is further reduced by more than a factor of two.

In the ion cyclotron range of frequency fast wave experiment, ion Bernstein waves may be excited inadvertently through the E_z or B_θ rf field. In the present work we have demonstrated in a hydrogen plasma that electrostatic wave excitation can occur in a good range of wave frequencies: for $0.2\ \Omega_i < \omega < \Omega_i$, the cold electrostatic ion cyclotron wave (Sec. IIIB), and for $\Omega_i < \omega \lesssim 3\ \Omega_i$ the ion Bernstein wave. If the electrostatic waves are excited at an appreciable amplitude, they will change the plasma loading of the induction coil (or coupling of waveguide antenna) and, also, can cause unexpected effects on the plasma such as the edge plasma heating. Electrostatic excitation can arise in a number of situations through 1) leakage in the Faraday shield, 2) induction-coil alignment error $\sim B_p/B_o$, inducing a significant level of $E_\parallel$-field, or 3) linear and non-linear interactions of high-power rf with the edge plasma. The expected level of excitation may be larger if a waveguide launcher without Faraday shield is employed or if the heat load and material erosion considerations in a reactor situation necessitate the elimination of the Faraday shield outside a conventional induction coil. For these reasons, it is of interest to understand the physics of electrostatic wave excitation in the ion cyclotron range of frequencies and to make proper assessment of the level of excitation and its consequences. Also in the fast wave heating experiment, under

certain conditions,[2-6] the ion Bernstein waves are believed to be excited via a linear mode-conversion process where the subsequent propagation (and damping) property of the converted ion Bernstein waves can determine the heating characteristics of the fast wave heating.

Finally, the excellent coherence of the externally launched ion Bernstein wave together with its strong dependence on the local hydrogen ion temperature offers an interesting T_i diagnostic possibility[24] for future fusion devices where such measurements become increasingly difficult. The present method can be implemented with existing microwave and/or laser scattering technology[25-27] in tokamak plasmas enabling local T_i measurement through the externally launched ion Bernstein wave dispersion relation.

Experiments are being planned in ACT-1 to investigate possible non-linear effects associated with high-power rf on ion Bernstein wave excitation.

ACKNOWLEDGMENTS

The authors would like to thank T. H. Stix and W. M. Hooke for helpful discussions and for their continued interest in the present work. Thanks are also due to J. Taylor and W. Kineyko for their valuable technical assistance.

This work was supported by the U.S. Department of Energy Contract No. DE-AC02-76-CHO3073.

REFERENCES

1. T. H. Stix, Phys. Rev. Lett. 15, 878 (1965).
2. D. G. Swanson and Y. C. Ngan, Phys. Rev. Lett. 35, 517 (1975).
3. J. Jacquinot, B. D. McVey, and J. E. Scharer, Phys. Rev. Lett. 39, 88 (1977).
4. F. W. Perkins, Nucl. Fusion 17, 1197 (1977).
5. H. Takahashi et al., Phys. Rev. Lett. 39, 31 (1977).
6. J. Hosea et al., Phys. Rev. Lett. 42, 1803 (1979).
7. S. Puri, Phys. Fluids 22, 1716 (1979).
8. M. Ono, Princeton Plasma Physics Laboratory Report No. 1593, 1979.
9. M. Ono, R. Horton, T.H. Stix, and K. L. Wong, in Proceedings of the 2nd Joint Grenoble-Varenna International Symposium of Heating in Toroidal Plasmas (Commission of the European Communities. Directorate-General XII-Fusion Programme. Brussels, 1980) Vol. I, p 593.
10. M. Ono and K. L. Wong, Phys. Rev. Lett. 45, 1105 (1980).
11. T. H. Stix, Theory of Plasma Waves (McGraw-Hill, New York, 1962), p. 226.
12. P. M. Bellan and M. Porkolab, Phys. Fluids, 17, 1592 (1974).
13. M. Brambilla, Plasma Physics 18, 669 (1976). (This also gives references to earlier works on mode-conversion).
14. D. G. Swanson, Phys. Fluids 10, 1531 (1975).

15. R. K. Fisher and R. W. Gould, Phys. Fluids 14, 857 (1971).

16. K. L. Wong and M. Ono, Bull. Am. Phys. Soc. 24, 957 (1979).

17. M. Ono, Phys. Rev. Lett. 42, 1267 (1979).

18. R. J. Briggs and R. W. Gould, Phys. Fluids 14, 857 (1971).

19. P. M. Bellan and M. Porkolab, Phys. Rev. Lett. 34, 124 (1975).

20. M. Ono, M. Porkolab, and R. P. H. Chang, Phys. Fluids 23, 1656 (1980).

21. J. P. M. Schmitt, Phys. Rev. Lett. 31, 982 (1973).

22. K. L. Wong, R. Horton and M. Ono, Phys. Rev. Lett. 45, 117 (1980).

23. N. J. Fisch, Phys. Rev. Lett. 41, 873 (1978).

24. G. A. Wurden, M. Ono, K. L. Wong, and A. Semet, Bull. Am. Phys. Soc. 25, 938 (1980).

25. E. Mazzucato, Phys. Rev. Lett. 36, 792 (1976).

26. C. M. Surko and R. E. Slusher, Phys. Rev. Lett. 37, 1747 (1976).

27. W. A. Peebles, N. C. Luhmann, Jr., A. Mase, H. Park, and H. Semet, Rev. Sci. Instrum., 52, 360 (1981).

FIGURE CAPTIONS

Fig. 1. Behavior of wave dispersion relation near the lower hybrid resonance layer (b=0). The solid curve shows mode-transformation process for $\omega < 2\Omega_i$ (a>0). The dashed curve shows mode-conversion process for $\omega >> \Omega_i$ (a<0).

Fig. 2. Mode-transformation at second harmonic frequency. (a) Wave number vs radial distance in a hydrogen plasma with a linear rise in density. Ion temperatures as labeled, f = 11.85 MHz, ω/Ω_H (x=0) = 1.9, λ_n = 36 cm, n_e(b=0) = 2.3×10^9 cm^{-3}. (b) Wave trajectories for the case shown in (a). Wave exciter is placed at x = 0 cm.

Fig. 3. Mode-transformation at higher harmonic frequencies. (a) Wavenumber vs radial distance for various ion temperatures (as labeled) for $\omega \lesssim 3\Omega_i$ excitation in a hydrogen plasma, f = 18.1 MHz, ω/Ω_H (x=0) = 2.9, λ_n = 36 cm, n_e(b=0) = 6×10^9 cm^{-3}. (b) Wave trajectories for the case shown in (a). (c) Wavenumber vs radial distance for various ion temperature (as labeled) for $\omega \lesssim 4\Omega_i$ excitation, f = 24.3 MHz, ω/Ω_H (x=0) = 3.9, λ_n = 36 cm, n_e(b=0) = 1.26×10^{10} cm^{-3}. (d) Wave trajectories for the case shown in (c).

Fig. 4. Schematic of the experimental set-up.

Fig. 5. Schematic of the tungsten filament plasma source.

Fig. 6. Radial plasma profiles in ACT-1 (a) Radial density profile (b) Electron and ion temperature profiles. Plasma center is at r = 0 cm, $P_H = 7 \times 10^{-6}$Torr.

Fig. 7. Hydrogen ion concentration measurement by low-frequency resonance-cone propagation. (a) Radial amplitude profiles of low frequency resonance cone. Top trace is for the antenna placed three ports away and the bottom trace is for six ports away. (b) Frequency vs measured cone angle normalized by the square root of electron-ion mass ratio.

Fig. 8. Radial profiles of wave amplitude for various axial positions, z(as labeled). Dashed curves are calculated trajectories. Antenna-limiter position is at x = 0 cm. The lower hybrid resonance is at x = 1 cm.

Fig. 9. Ion Bernstein wave identification. (a) Interferometer traces. Parameters on each curve are ω/Ω_H (x=2 cm), f = 12-13 MHz, B_o(x=2 cm) ≃ 4.3 kG, and antenna-limiter position at x = 0 cm. (b) Interferometer trace for various time delays, Δt or the phase delay in unit of 2π. Parameter on curves is $\omega\Delta t/2\pi$. (c) Wave dispersion relation. Dots are experimental points and solid curves are the theoretical values obtained for various ion temperatures. $P_H = 7 \times 10^{-6}$Torr, $n_e \simeq 10^{10}$ cm^{-3}, x = 4 cm.

Fig. 10. Ion Bernstein wave radial phase front. (a) Radial interferometry trace for various vertical positions. Antenna-limiter is at r = 5.9 cm, antenna vertical height, h = 6.3 cm. The plasma minor axis is at r = 0, h = 0, (b) Radial phase front obtained from Fig. 10(a).

Fig. 11. Radial wave amplitude vs antenna phasing ϕ (as labeled). Solid trace is the measured wave amplitude and dashed trace is interferogram output. Calculated radial positions are indicated in the top for various $\lambda_{\parallel}$-component.

Fig. 12. Launching of unidirectional ion Bernstein wave by $\phi = \pm \pi/2$ antenna phasing. (a) Schematic of launching configuration. (b) Detected wave amplitude. Top and bottom traces are for waves being launched toward and away from a detecting probe, respectively.

Fig. 13. Mode-transformation process. (a) Radial interferometry traces for various neutral pressures. (b) Wavenumber vs radial position. Dots are experimental points and curves are theoretical values. Antenna-limiter is at x = 0 cm, ω/Ω_H (x=0) = 1.92, $P_H = 7 \times 10^{-6}$Torr.

Fig. 14. Wave packet trajectory vs plasma density. (a) Radial wave packet amplitude profiles (thicker curve) and interferogram traces (finer curve) measured at six ports away ($\Delta z \simeq 90$ cm) for various

central densities (as labeled). $P_H = 8.5 \times 10^{-6}$Torr, $f = 12.5$ MHz and $B_o = 4.7$ kG. (b) Corresponding wave packet position as predicted from ray-tracing calculation for various $\lambda_{\parallel}$.

Fig. 15. Third harmonic launching of IBW. (a) $\omega \lesssim 3\Omega_i$ IBW dispersion relation. Dots are measured and solid curves are theoretical values for various T_i (as labeled). $B_o = 4.3$ kG, $r = 4$ cm, $n_o \simeq 3 \times 10^{10}$ cm^{-3}. (b) Wavenumber vs radial distance from the antenna. Dots are experimental points and curves are theoretical values. Lower hybrid resonance layer is indicated by a dashed line.

Fig. 16. Ion temperature at $r = 3$ cm obtained from ion Bernstein wave dispersion relation vs neutral hydrogen filling pressure.

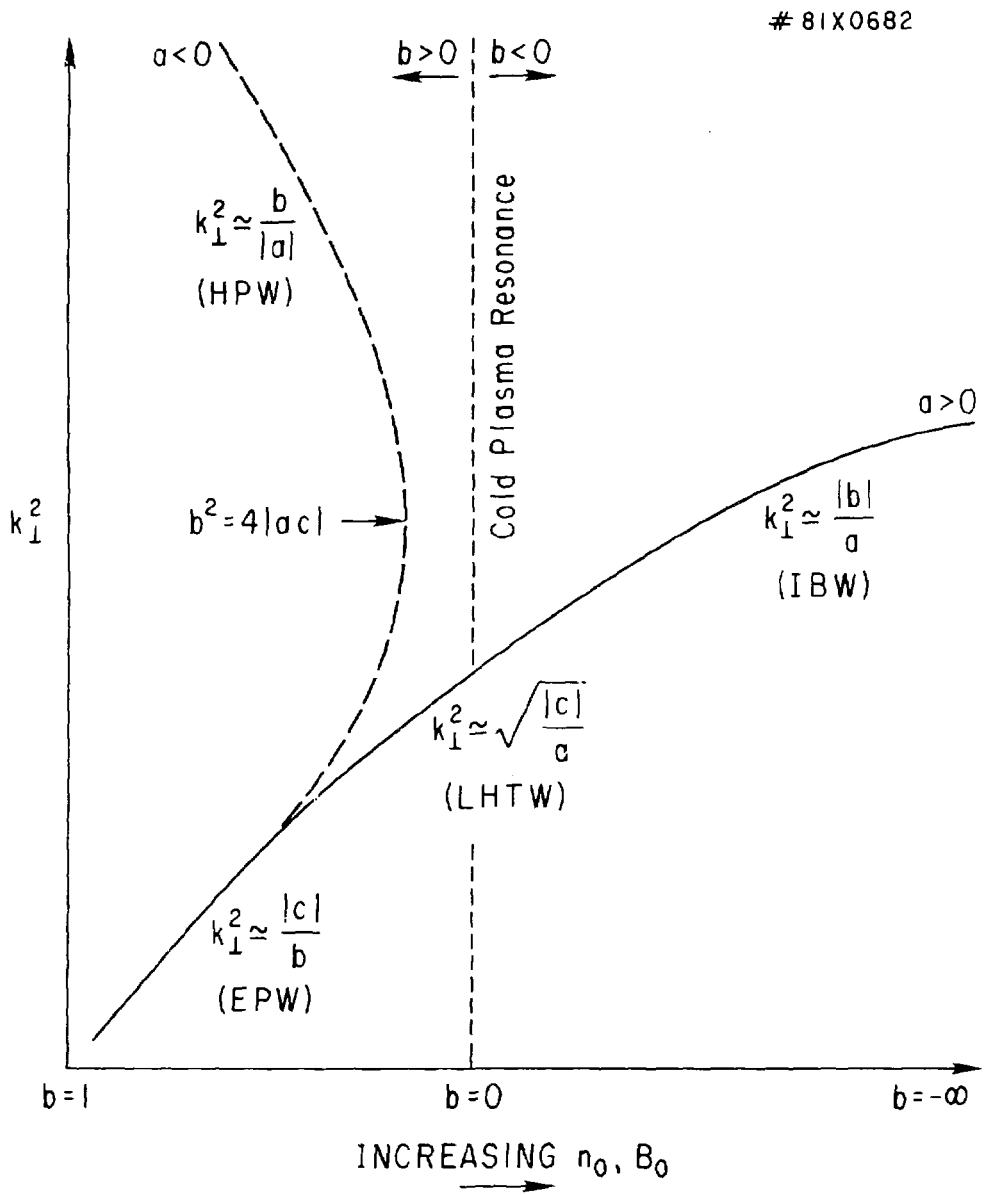
#81X0682
a<0
b>0
b<0
$k_\perp^2 \simeq \frac{b}{|a|}$
(HPW)
Cold Plasma Resonance
a>0
$k_\perp^2$
$b^2 = 4|ac|$
$k_\perp^2 \simeq \frac{|b|}{a}$
(IBW)
$k_\perp^2 \simeq \sqrt{\frac{|c|}{a}}$
(LHTW)
$k_\perp^2 \simeq \frac{|c|}{b}$
(EPW)
b=1
b=0
b=-∞
INCREASING n_0, B_0

Fig. 1

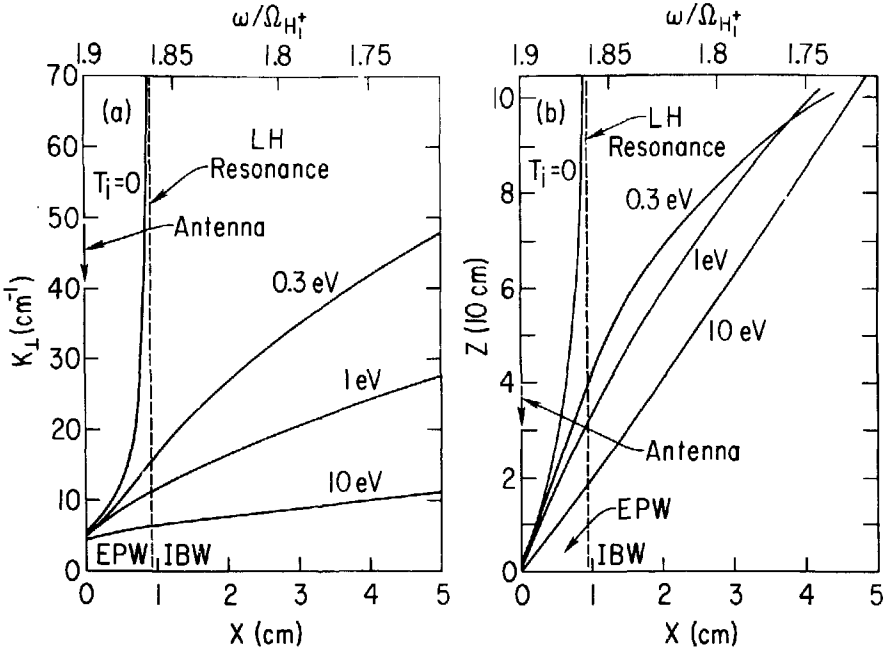
ω/Ω_H1+
1.9
1.85
1.8
1.75
(a)
LH
Resonance
T_i=0
Antenna
0.3 eV
1 eV
10 eV
EPW
IBW
K⊥ (cm⁻¹)
X (cm)
(b)
Z (10 cm)

Fig. 2

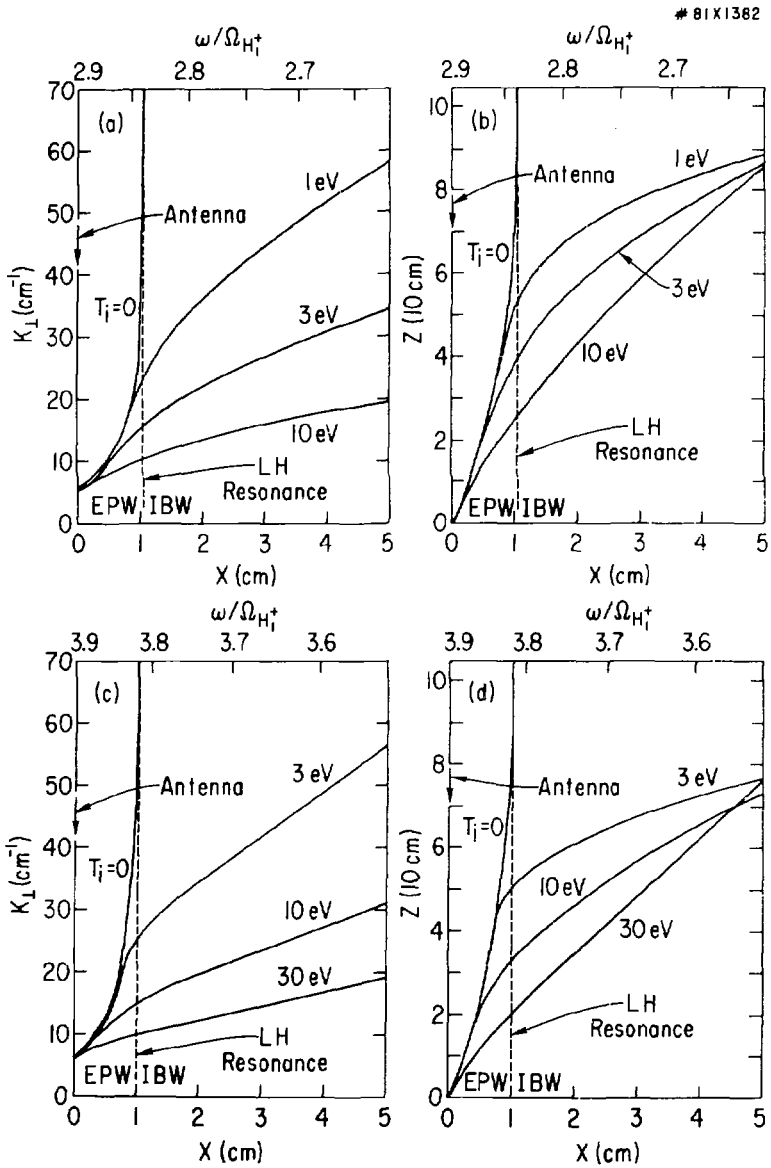
#81X1382
ω/Ω_H1+
2.9
2.8
2.7
(a)
Antenna
1eV
3eV
10eV
T_i=0
LH
Resonance
EPW
IBW
K⊥(cm⁻¹)
X (cm)
(b)
Z (10 cm)
3.9
3.8
3.7
3.6
(c)
30eV
(d)

Fig. 3

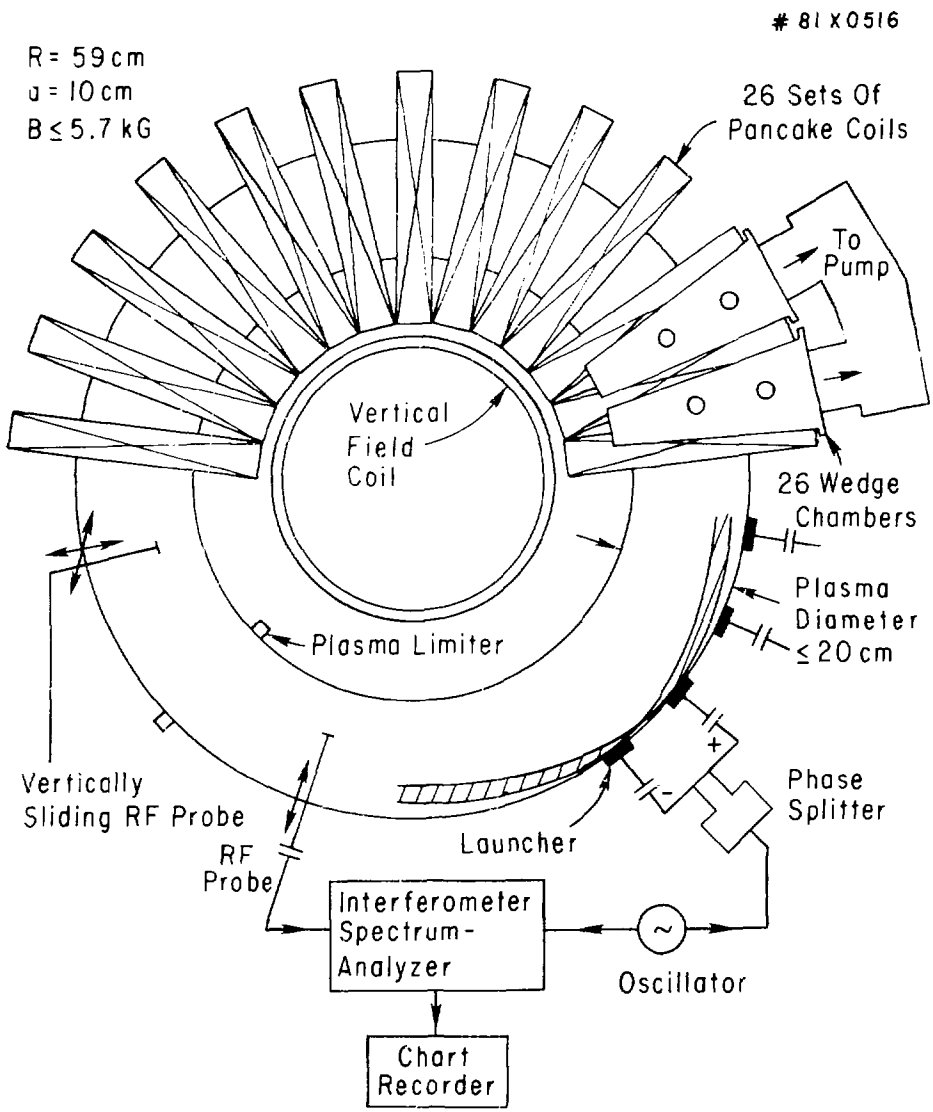
#81X0516
R = 59 cm
a = 10 cm
B ≤ 5.7 kG
26 Sets Of
Pancake Coils
To
Pump
Vertical
Field
Coil
26 Wedge
Chambers
Plasma
Diameter
≤ 20 cm
Plasma Limiter
Vertically
Sliding RF Probe
RF
Probe
Launcher
Phase
Splitter
Interferometer
Spectrum-
Analyzer
Oscillator
Chart
Recorder

Fig. 4

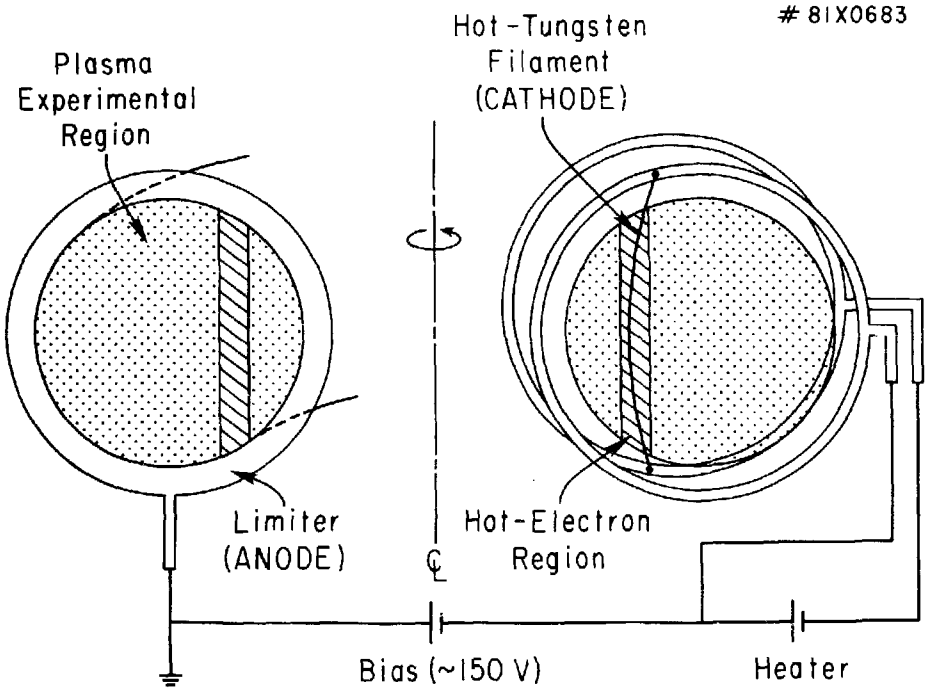
#81X0683
Hot-Tungsten
Filament
(CATHODE)
Plasma
Experimental
Region
Limiter
(ANODE)
Hot-Electron
Region
Bias (~150 V)
Heater

Fig. 5

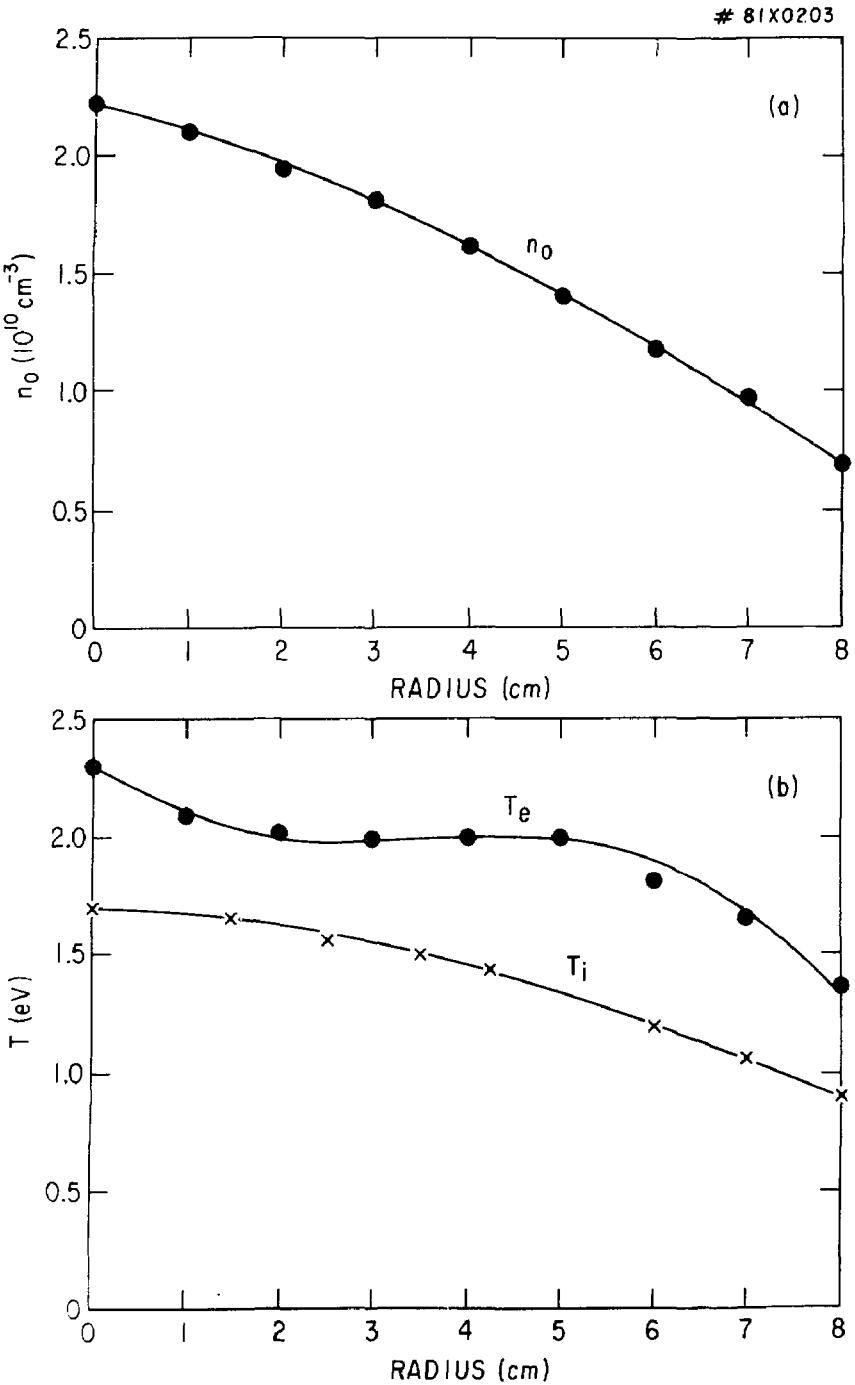

Fig. 6

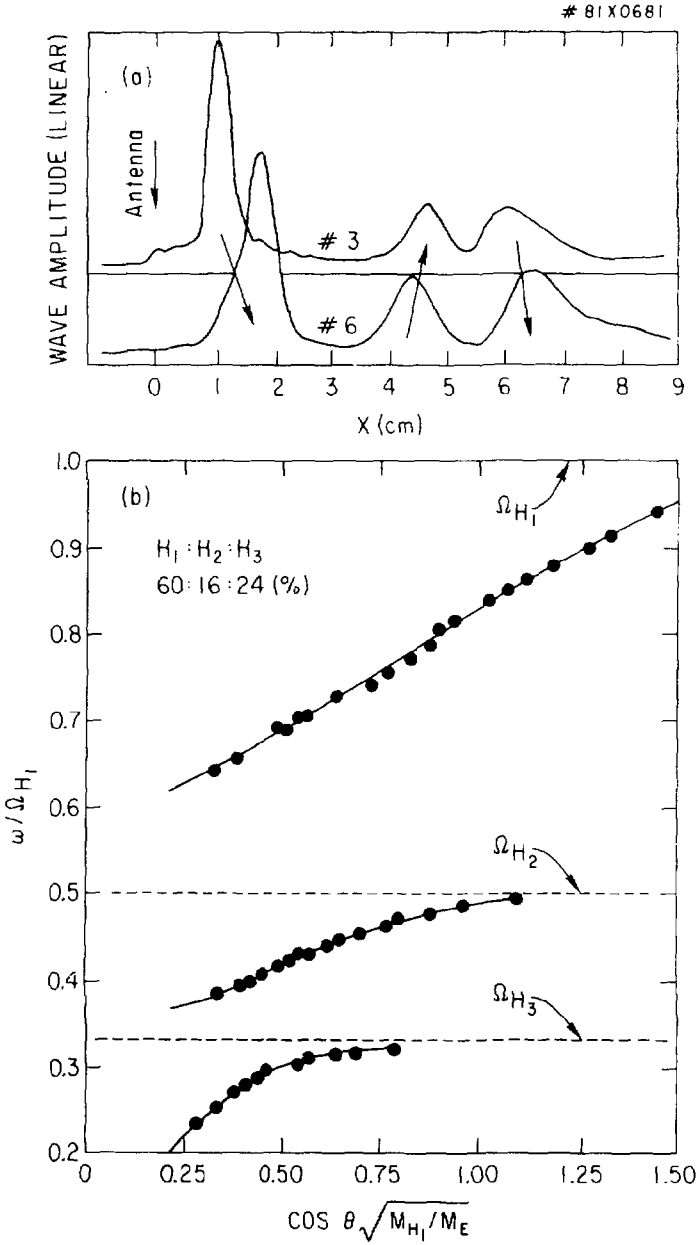
81X0681
(a)
Antenna
WAVE AMPLITUDE (LINEAR)
3
6
0 1 2 3 4 5 6 7 8 9
X (cm)
(b)
$H_1 : H_2 : H_3$
60 : 16 : 24 (%)
Ω_{H_1}
Ω_{H_2}
Ω_{H_3}
ω / Ω_{H_1}
1.0 0.9 0.8 0.7 0.6 0.5 0.4 0.3 0.2
0 0.25 0.50 0.75 1.00 1.25 1.50
COS $\theta \sqrt{M_{H_1}/M_E}$

Fig. 7

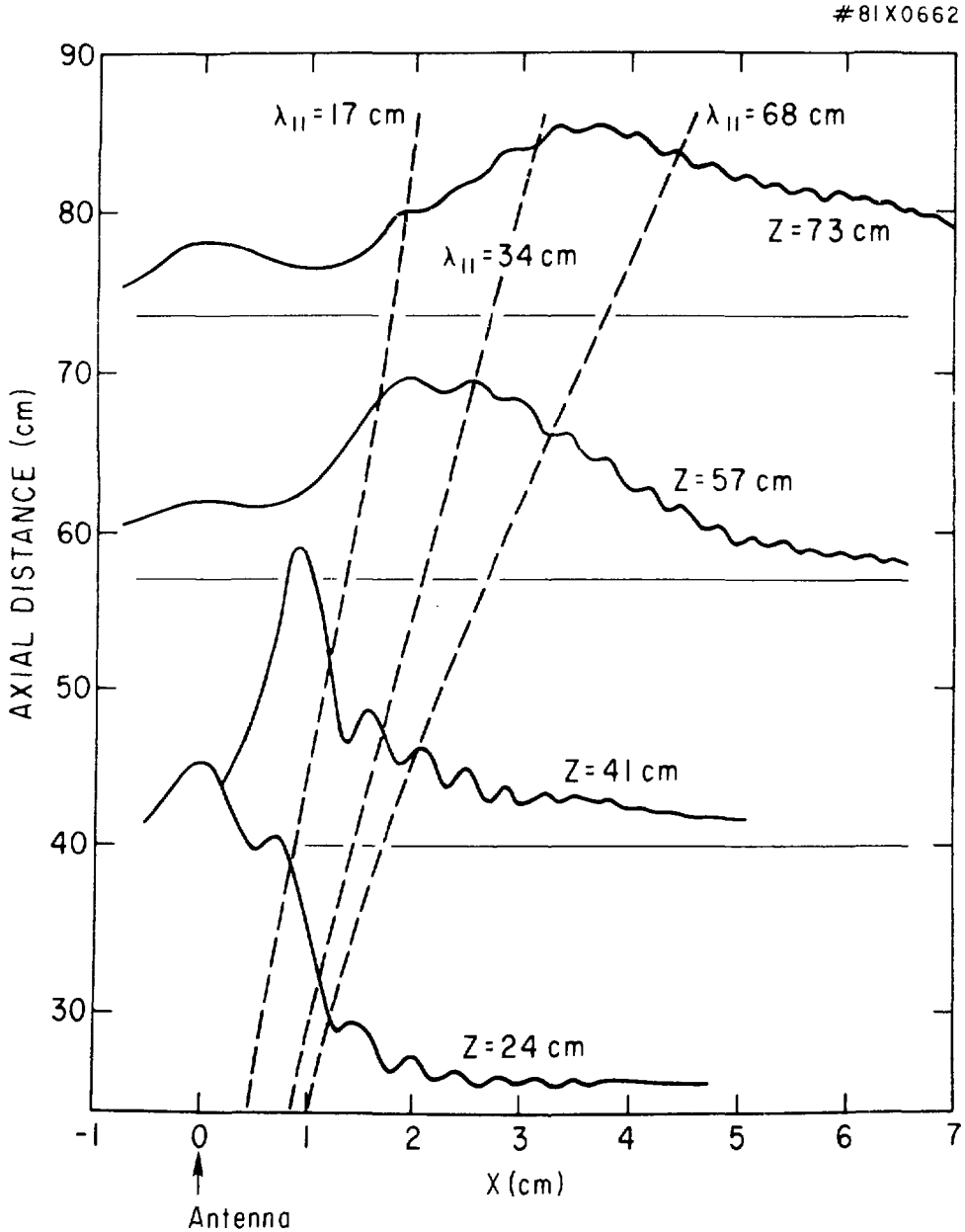
#81X0662
λ11 = 17 cm
λ11 = 34 cm
λ11 = 68 cm
Z = 73 cm
Z = 57 cm
Z = 41 cm
Z = 24 cm
AXIAL DISTANCE (cm)
X (cm)
Antenna
90
80
70
60
50
40
30
-1
0
1
2
3
4
5
6
7

Fig. 8

#81X0664

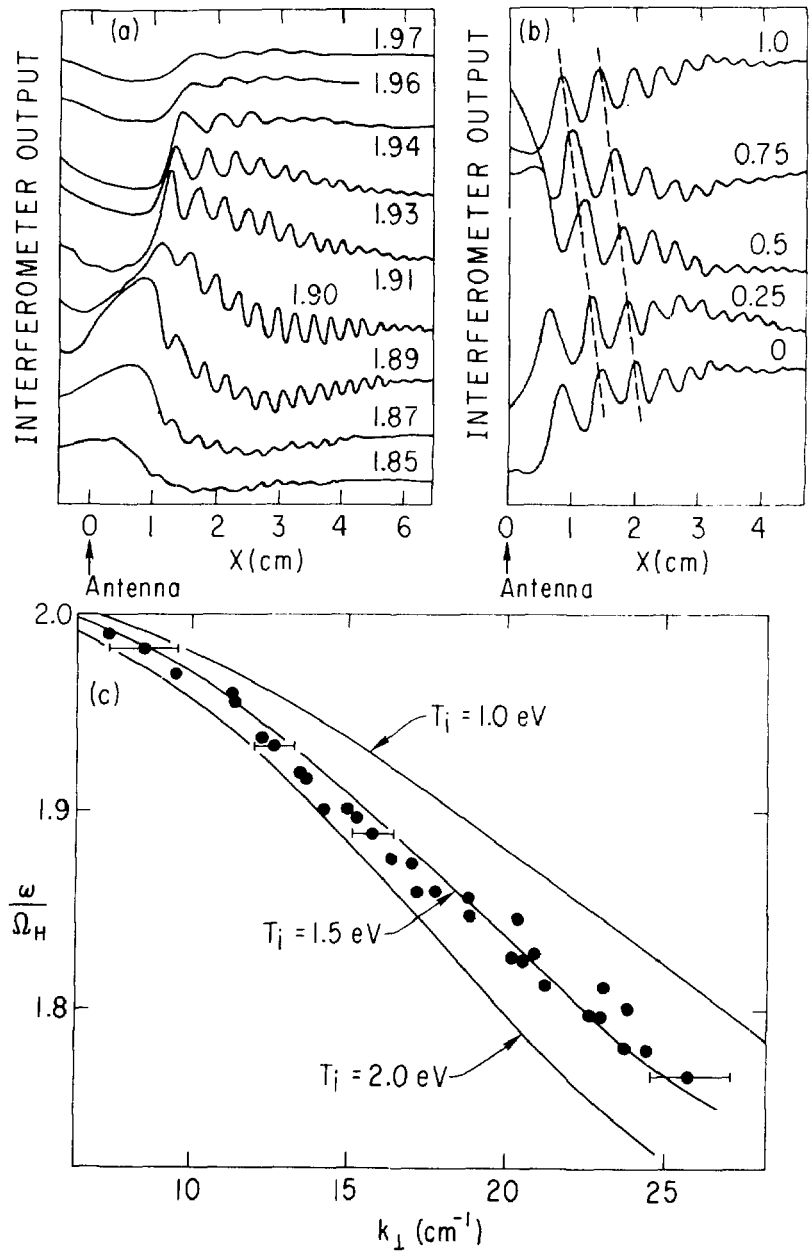

Fig. 9

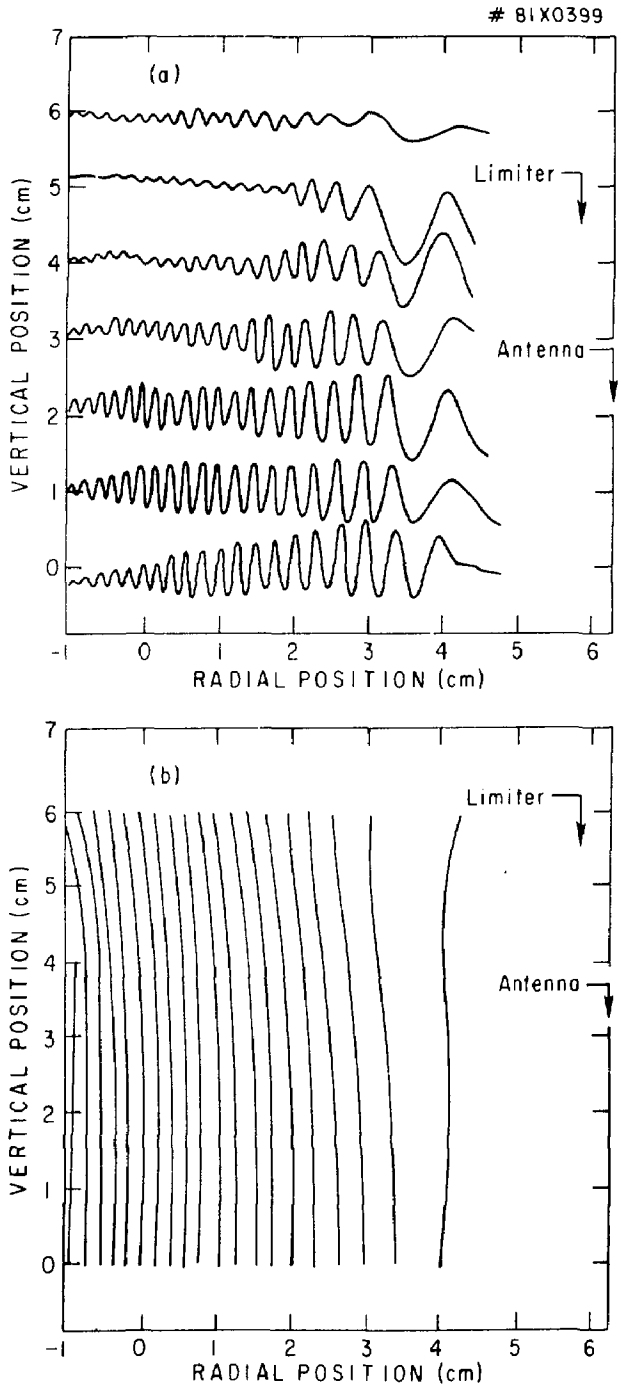
81X0399
(a)
Limiter
Antenna
VERTICAL POSITION (cm)
RADIAL POSITION (cm)
(b)
Limiter
Antenna
VERTICAL POSITION (cm)
RADIAL POSITION (cm)

Fig. 10

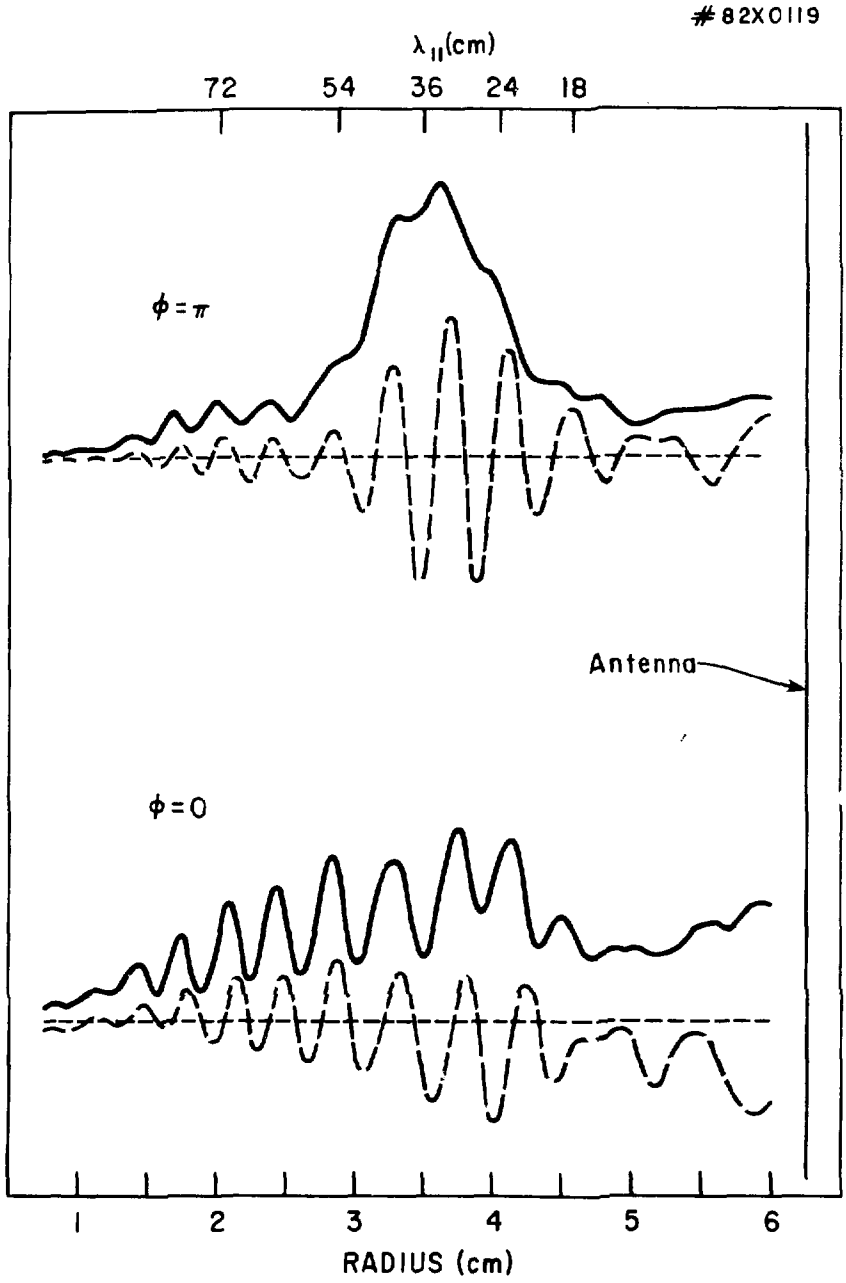
#82X0119
$\lambda_{\parallel}$(cm)
72
54
36
24
18
$\phi = \pi$
Antenna
$\phi = 0$
1
2
3
4
5
6
RADIUS (cm)

Fig. 11

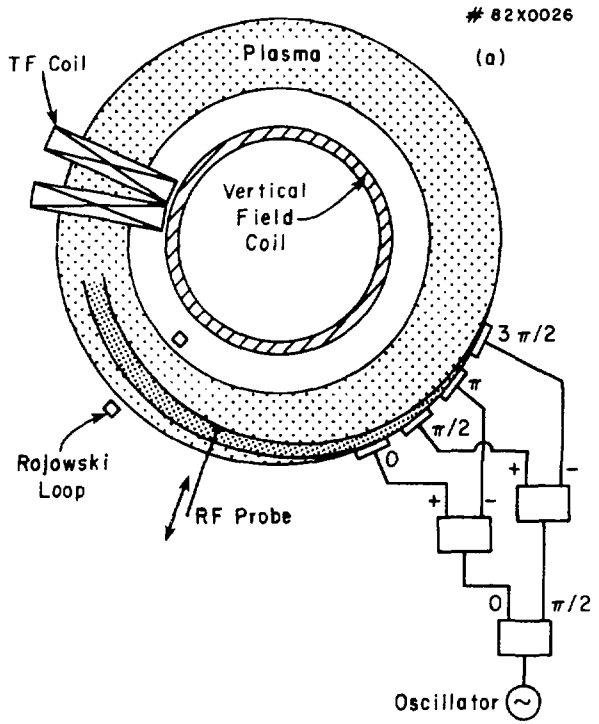
82X0026
(a)
TF Coil
Plasma
Vertical
Field
Coil
3 π/2
π
π/2
0
Rojowski
Loop
RF Probe
+
-
+
-
0
π/2
Oscillator

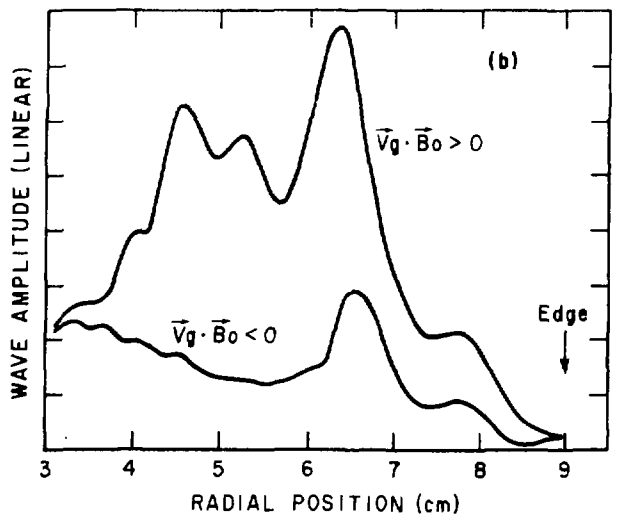
(b)
WAVE AMPLITUDE (LINEAR)
$\vec{V}g \cdot \vec{B}o > 0$
$\vec{V}g \cdot \vec{B}o < 0$
Edge
3
4
5
6
7
8
9
RADIAL POSITION (cm)

Fig. 12

#81X0663

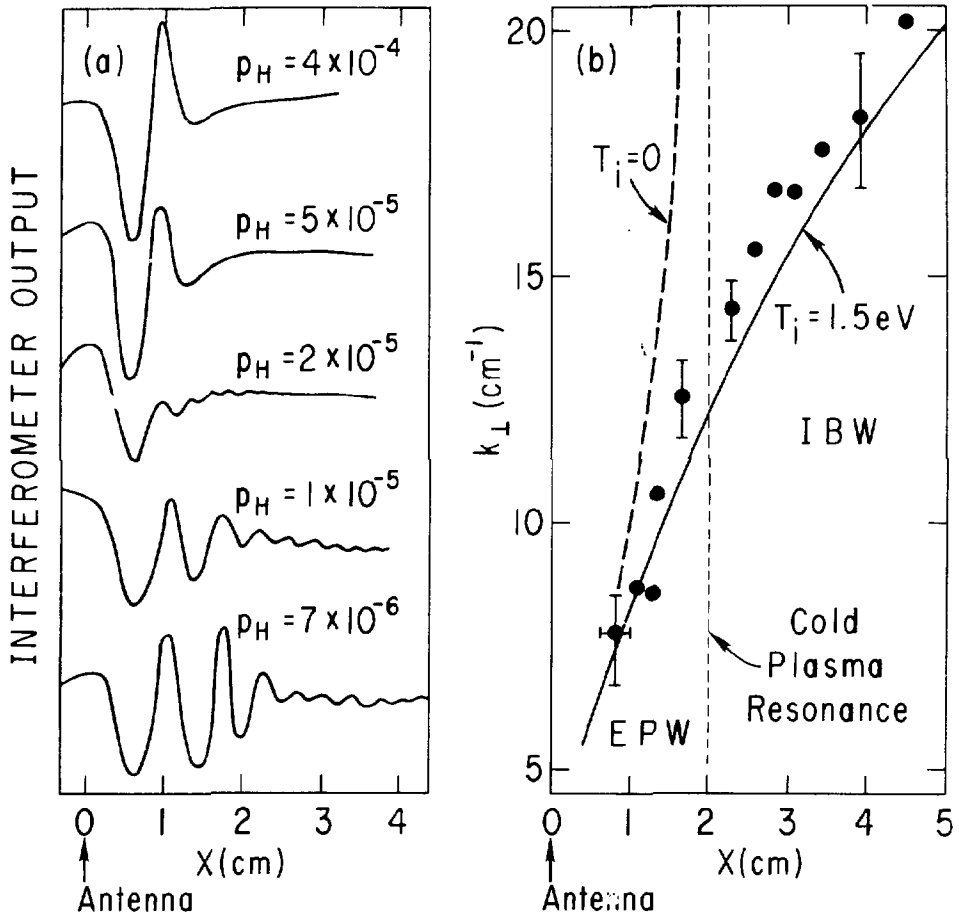

Fig. 13

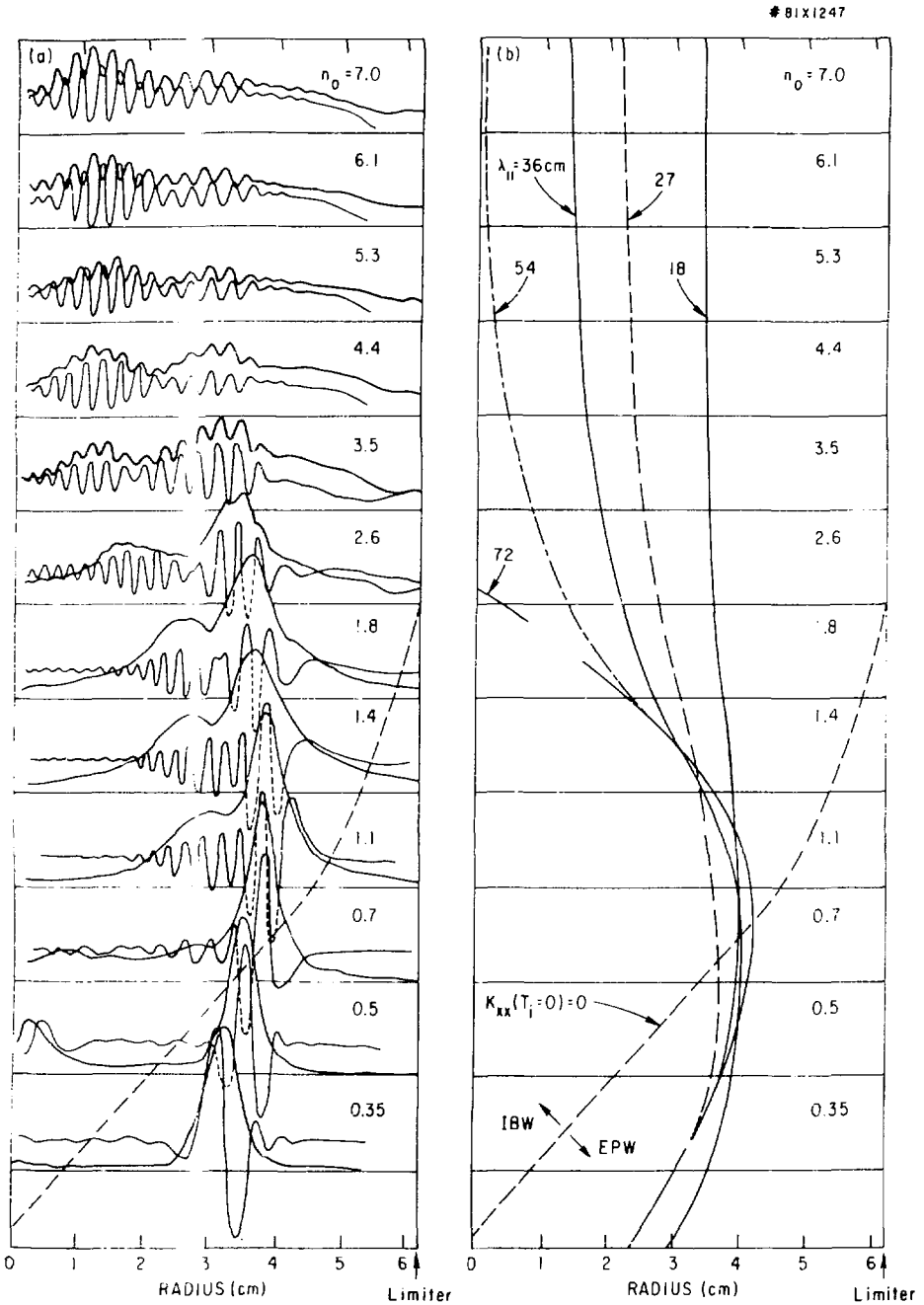
#81X1247
(a)
n_0 = 7.0
6.1
5.3
4.4
3.5
2.6
1.8
1.4
1.1
0.7
0.5
0.35
0 1 2 3 4 5 6
RADIUS (cm)
Limiter
(b)
n_0 = 7.0
$\lambda_{\parallel}$ = 36cm
27
54
18
72
$K_{xx}(T_i=0)=0$
IBW
EPW
RADIUS (cm)
Limiter

Fig. 14

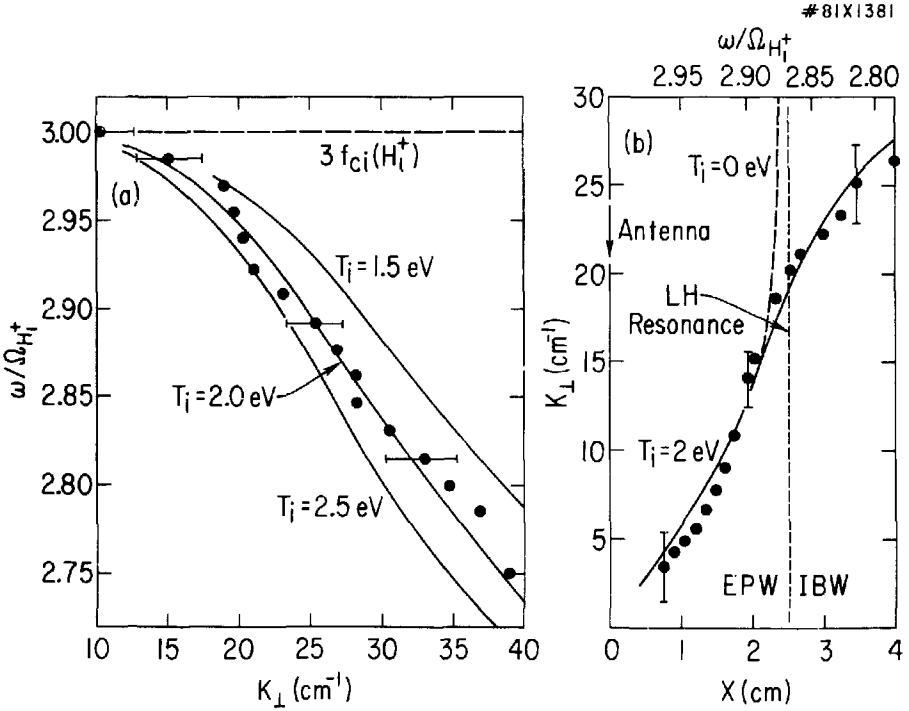
#81X1381
(a)
3 fci(H1+)
Ti = 1.5 eV
Ti = 2.0 eV
Ti = 2.5 eV
ω/ΩH1+
K⊥ (cm-1)
(b)
Ti = 0 eV
Antenna
LH
Resonance
Ti = 2 eV
EPW
IBW
X (cm)

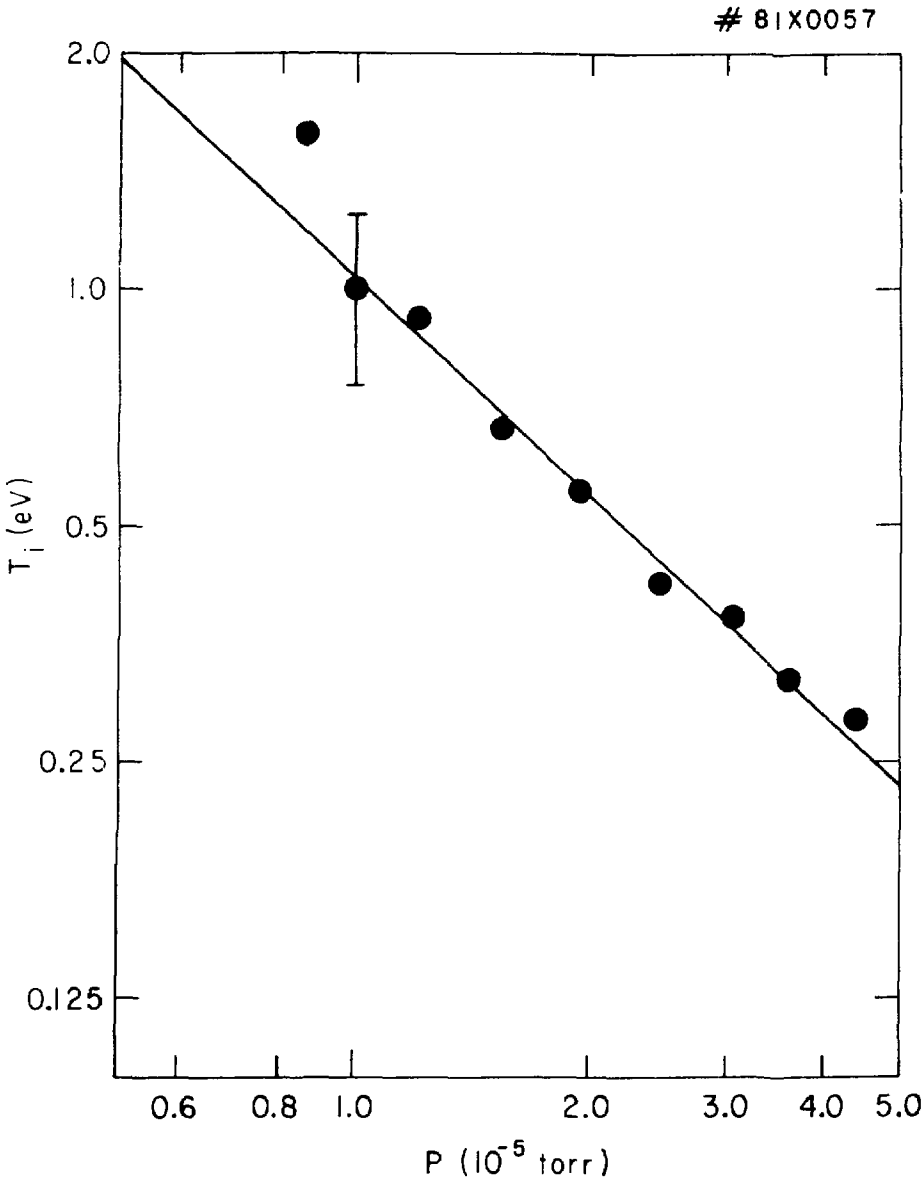

Fig. 16